First approach for modelling the physical foaming of tannin-based thermoset foams

Z. Marie, Nicolas Vincent, A. Celzard, V. Fierro

First approach for modelling the physical foaming of tannin-based thermoset foams

Z. Marie[a], V. Nicolas[a], A. Celzard[a], V. Fierro[a]

[a] Université de Lorraine, CNRS, IJL, F-88000 Epinal, France

Abstract

In the present paper, the foaming process of biosourced thermoset foams was considered at the lab scale with the aim of creating a numerical model able to simulate, for the first time, their manufacturing process. A multi-physical model was thus generated, having as driving force of the expansion the inner gas pressure of the foam, calculated from mass, heat and mechanical balances. In addition, and this is another originality of our work, the study was implemented in a 2D axisymmetric mobile mesh. The simulation was not stopped just after the rise of temperature and the related material expansion but, instead, a complete simulation of the whole process was offered, i.e., including cooling. Simulated and experimental data such as temperature changes and foam growth were compared, and a fair agreement was observed, suggesting the relevance of our approach.

Keywords: Porous media; simulation; foaming process; heat and mass transfers; tannin

Corresponding Author: vincent.nicolas@univ-lorraine.fr

1 Introduction

Rigid foams find applications in various sectors due to their unique combination of thermal, acoustic and mechanical properties, associated with a very low bulk density. Construction and transportation industries are major examples in which such materials are widely used. Most of these foams are thermoset, whose market is dominated by three polymers: polyurethane, phenolic and epoxy [1] and, for preparing them, two different processes are possible, chemical and physical foaming. Chemical foaming consists in producing a gas from the polymerisation reaction(s). Thus, polyurethane generally expands due to the carbon dioxide formed by the reaction between isocyanate and water [2]. However, physical foaming is also possible, by which a vapour is produced from the sudden evaporation of a low boiling point-liquid phase purposely added to the formulation, for instance pentane [3].

In the recent past, bio-based foams obtained from one or the other process, were reported, i.e., either by chemical foaming [4] or physical foaming [5], and even by mixed foaming [6]. The purpose of these new cellular solids was to compete with synthetic foams in terms of properties while using greener raw materials. Similarly, biosourced polyurethane foams were shown to present similar or better performances than those of synthetic foams while being more environment-friendly and valorising at the same time some wastes from agriculture and food industries [7]. The polyurethane industry indeed investigated the incorporation of different types of plant polyols derived from castor oil [8], soybean oil [9], palm oil, rapeseed oil and linseed oil [10], safflower oil [11], coffee grounds, lignin [12] or wheat straws [8–14]. Others alternatives aimed at substituting traditional phenolic reagents by biosourced extracts [15], such as those used in the present work: tannins.

Whether thermoset foams are purely synthetic or bio-based, better understanding their formation would be quite useful. It would allow not only optimising them further, but also skipping the heavy experimental design that is required as soon as some changes in the preparation process are made (e.g. in terms of volume of formulation, nature of the moulds, processing temperature, etc.). The material's expansion indeed critically depends on the heat generated by the polymerisation in the case of physical blowing, and the amount of heat that can be retained in the bulk of the formulation and used for foaming is related to the amount of polymer, to the losses throughout the walls of the mould, and to the outside temperature.

Modelling the foaming of thermoset polymers might be done through a numerical approach. Several models have already been implemented, most of them in 0D geometry [2,3,16–20], 2D [21,22] but also in 3D [23–27]. 0D simulations calculate one temperature and a total density for a macroscopic approach on the one hand, and cells dimensions for a microscopic approach on the other hand. They do not allow estimating physical changes at different spatial points (e.g. temperature, pressure and local porosity), which would be interesting for processing big blocks of foam or for optimising their preparation, based on given boundary conditions. In general, 3D geometry simulations are implemented with a volume of fluid (VOF) method. But most of these models (0D and 3D) simulate the increase of temperature and the corresponding foam expansion without considering the end of the process, such as cooling and others phenomena like drying, shrinkage, etc.

In the present paper, simulating the foaming process of biosourced foams at the lab scale was considered for the first time. These materials are derived from mimosa tannin, a

polyphenolic vegetable extract, polymerised in the presence of furfuryl alcohol as co-reagent, water as solvent, formaldehyde as crosslinker, para-toluenesulphonic acid as catalyst, and diethyl ether as (physical) blowing agent. Their preparation, chemistry and properties were abundantly detailed elsewhere [28–34], and the aim of the present work was thus to create a numerical model able to simulate, for the first time, their manufacturing process. From such model, quantifying the impact of each phenomenon taking place during the foaming process was expected. A multi-physical model was thus generated, having as driving force of the expansion the gas pressure inside the foam, calculated from mass, heat and mechanical balances. In addition, and this is another originality of our work, the study was implemented in a 2D axisymmetric mobile mesh. Finally, the simulation was not stopped just after temperature increase and related material expansion but, instead, a complete simulation of the whole process was offered, including cooling.

Such a model is thus presented below. First, the experimental part is detailed. Then, the physics and the coupling between the involved physical phenomena are considered, and how the numerical simulation was carried out is explained. Regarding the latter, a parametric study was proposed for choosing the most relevant mesh parameters. Finally, the numerical results are compared to the experimental ones, and the evolution of some physical properties of the foam during the foaming - cooling process is discussed.

2 Materials and methods

2.1 Formulation of the foam

The present foams are based on commercial mimosa tannin extract, available on the market under the name FINTAN-OP and kindly provided by SilvaChimica (St. Michele Mondovi, Italy). It should be noticed here that tannin was used as such, without any purification: this light-brown powder generally contains 80–82% of actual phenolic flavonoid materials, 4–6% of water, 1% of amino and imino acids, the remainder being monomeric and oligomeric carbohydrates, in general broken pieces of hemicelluloses. Mimosa tannin is soluble in water, and is generally composed of two up to eleven monomers flavonoid units. Therefore, this biopolymer is characterised by low molecular weights ranging typically from 500 to 3500 g mol^{-1}. More details can be found elsewhere [35].

Herein, the formulation presented in *Table 1* was used as follows. First, tannin extract was dissolved in water under strong mechanical stirring, and mixed with furfuryl alcohol. Then,

diethyl ether and a 37 wt. % aqueous formaldehyde solution were added, and the whole was thoroughly homogenised. The final addition of a 65 wt. % aqueous solution of para-toluenesulphonic acid (pTSA) immediately followed by stirring the as-obtained viscous resin led to its expansion after a few tens of seconds. Indeed, the auto-polymerisation of furfuryl alcohol as well as the co-reaction of tannin and furfuryl alcohol is highly exothermic, and the corresponding increase of temperature produced the boiling of the diethyl ether, and hence the foaming. At the same time, the formaldehyde crosslinked the polymer and stabilised the foam, turning it into a rigid cellular material so that no collapse occurred. The end of the process is characterised by an increase of mechanical properties and by the progressive cooling of the foam.

Table 1: Standard formulation of tannin-based foam

Ingredients and roles in the formulation	Mass (g)	Role in the mass conservation equation
Mimosa tannin extract; base of the resin	60	Skeleton
65% pTSA in water; acid catalyst	22	Skeleton
Furfuryl alcohol; co-reagent producing heat upon polymerisation	21	Skeleton
Formaldehyde (37% in water); crosslinker	14.8	Skeleton
Water; solvent	12	Skeleton
Diethyl ether; (physical) blowing agent	6	Liquid or gas

2.2 Experimental protocol and measurement methods

The experimental data of foam temperature and expansion as a function of time were retrieved from a former work carried out by our team in 2013 [34], based on the formulation detailed in *Table 1*, without need of additional experiments. Those data were obtained using a FOAMAT apparatus Model 281 (Foamat Messtechnik GmBH, Karlsruhe, Germany). With such a device, the liquid mixture described above was poured into a cylindrical cardboard mould (diameter 10 cm) in which the reaction took place. The expansion of the foam was monitored as a function of time by measuring the position of the top surface of the foam with a ventilated ultrasound sensor placed above the foam, and working in a pulse-echo mode. The temperature was measured with a K-type thermocouple whose position was maintained fixed 1.8 cm above the bottom of the mould and whose probe was centred on the vertical axis. With such a set of data, it is expected that the general trends derived from the model are verified as a first approximation, but no accurate validation is possible yet.

3 Multi-physical model

The porous foam structure was considered to be formed from an initially homogeneous medium comprising blowing agent (diethyl ether), able of phase change from liquid (subscript *de;l*) to gas (subscript *de;g*), and a "skeleton" phase (subscript *s*) corresponding to the rest of the ingredients (see *Table 1*), which all participate to polymerisation reactions and/or will be included in the solid resin. In other words, after foaming, all ingredients except the boiling agent will be part of the rigid foam. To consider as many phenomena as possible, the equations of mass, energy and momentum conservation were solved and completed with an equation accounting for the polymerisation reactions. As it is a first approach concerning the simulation of bio-sourced foams, the following phenomena will be neglected:

- diffusion of blowing agent into bubbles
- interfacial effects between gas and condensed phase
- wall-drainage and wall-rupture effects
- dependence of viscosity on the molecular architecture and concentration of prepared polymer and on the distribution of bubbles in the dispersion
- steps of bubble nucleation, growth and stabilisation.

The aforementioned simplifications are all related to the macroscopic character of the proposed model, and therefore cannot consider such details at its present stage of development.

3.1 Mass conservation

Changes of mass concentration, defined as the weights of the different phases divided by the total volume of the formulation at time *t*, were calculated from three mass conservation equations:

$$\frac{\partial \rho_{de;l}}{\partial t} + \frac{1}{r}\vec{\nabla} \cdot r\left(\rho_{de;l}\vec{u}\right) = K_{de} \qquad \text{Eq. 1}$$

$$\frac{\partial \rho_{de;g}}{\partial t} + \frac{1}{r}\vec{\nabla} \cdot r\left(\rho_{de;g}\vec{u}\right) = -K_{de} \qquad \text{Eq. 2}$$

$$\frac{\partial \rho_{s}}{\partial t} + \frac{1}{r}\vec{\nabla} \cdot r\left(\rho_{s}\vec{u}\right) = 0 \qquad \text{Eq. 3}$$

where *r* is the radial coordinate, $\rho_{de;l}$ and $\rho_{de;g}$ are mass concentrations of liquid and gaseous diethyl ether, respectively, and ρ_s is the mass concentration of the skeleton. The volume

fractions of each phase were defined as the ratios between mass concentrations ρ (numerically calculated) and intrinsic densities ρ^i, and read:

$$\varepsilon_s = \frac{\rho_s}{\rho_s^i}; \varepsilon_{de;l} = \frac{\rho_{de;l}}{\rho_{de;l}^i}; \varepsilon_{de;g} = \frac{\rho_{de;g}}{\rho_{de;g}^i}, \text{ with } \varepsilon_s + \varepsilon_{de;l} + \varepsilon_{de;g} = 1 \qquad \text{Eq. 4}$$

The intrinsic density of gaseous diethyl ether was calculated from the ideal gas law:

$$\rho_{de;g}^i = \frac{P_{de} M_{de}}{RT} \qquad \text{Eq. 5}$$

where P_{de} and M_{de} are pressure and molecular weight of gaseous diethyl ether, respectively, R and T being the molar gas constant and the absolute temperature, respectively.

In Eqs (1)-(3), $\vec{u}$ is the local expansion velocity, and K_{de} is a function related to the change of phase of diethyl ether which depends on the local temperature. Diethyl ether was assumed either a liquid or a gas below or above the corresponding boiling point T_{de} of the pure compound at atmospheric pressure, respectively. The phase change was simulated with a sigmoid function $f(T)$, centred on T_{de}, which takes values from 0 to 1 below and above T_{de}, respectively, within a range temperature ΔT. In addition, the contribution of other compounds to the vapour-liquid equilibrium was neglected (e.g., water, formaldehyde and furfuryl-alcohol). K_{de} thus reads:

$$K_{de} = -\rho_{de;l}^{st} \frac{\partial f(T)}{\partial t} = -\rho_{de;l}^{st} \frac{\partial f(T)}{\partial T} \frac{\partial T}{\partial t} \qquad \text{Eq. 6}$$

where $\rho_{de;l}^{st}$ represents the mass concentration of liquid diethyl ether able of phase change in the deformable matrix. This is an appendix variable that does not participate to the mass balance. In the case of a rigid matrix, this quantity is intuitively constant and takes the value of the mass concentration of liquid diethyl ether at t = 0 ($\rho_{de;l;0}$). But in the case of a deformable matrix, this quantity changes with the deformation and is thus calculated from a partial differential equation integrating the deformation:

$$\frac{\partial \rho_{de;l}^{st}}{\partial t} + \frac{1}{r} \underset{\mathrm{r}}{\nabla} \cdot r \left(\rho_{de;l}^{st} \underset{\mathrm{r}}{u} \right) = 0 \qquad \text{Eq. 7}$$

To facilitate the numerical resolution of Eq. (6), the derivative of the function *f(T)* was not solved. The following function was thus used instead [36]:

$$\frac{\partial f(T)}{\partial T} = \frac{1}{\sqrt{\pi\left(\frac{\Delta T}{4}\right)^2}} e^{\left(\frac{-(T-T_{de})^2}{\left(\frac{\Delta T}{4}\right)^2}\right)} \quad \text{Eq. 8}$$

3.2 Energy conservation

The temperature was calculated from the energy conservation equation as follows [25,37]:

$$\frac{\partial H}{\partial t} + \frac{1}{r}\overset{\mathrm{r}}{\nabla}\cdot r\left(\overset{\mathrm{r}}{Q} + H\overset{\mathrm{r}}{u}\right) = 0 \quad \text{Eq. 7}$$

where $\overset{\cup}{Q}$ is the conductive heat transfer calculated by Fourier's law:

$$\overset{\cup}{Q} = -\lambda\overset{\cup}{\nabla}T \quad \text{Eq. 8}$$

λ being the thermal conductivity of the foam during growth and H the total enthalpy, with embraces the enthalpy of each component, including temperature and phase-change contributions:

$$H = H_{de;l} + H_{de;g} + H_s \quad \text{Eq. 9}$$

$$H_{de;l} = \rho_{de;l} c_{p;de;l}\left(T - T_{ref}\right) \quad \text{Eq. 10}$$

$$H_{de;g} = \rho_{de;g}\left[c_{p;de;g}\left(T - T_{ref}\right) + L_{de}^{l\to g}\right] \quad \text{Eq. 11}$$

$$H_s = \rho_s\left[c_{p;s}\left(T - T_{ref}\right) + \xi\Delta H_{poly}\right] \quad \text{Eq. 12}$$

In these equations, c_p is the specific heat of each phase considered, T_{ref} the reference temperature, $L_{de}^{l\to g}$ the latent heat of vaporisation of diethyl ether, ξ the conversion (describing the progress of reaction which ranges from 0 when the reactions start to 1 when the polymerisation is completed), and ΔH_{poly} the (exothermic) enthalpy of polymerisation.

Finally, the temperature was calculated from the following equation (see the nomenclature section for the definition of the new terms):

$$\begin{aligned}&\left(\rho_{de;l}c_{p;de;l} + \rho_{de;g}c_{p;de;g} + \rho_s c_{p;s}\right)\frac{\partial T}{\partial t} + \frac{1}{r}\overset{\mathrm{r}}{\nabla}\cdot r\left(-\lambda\overset{\mathrm{r}}{\nabla}T + H\overset{\mathrm{r}}{u}\right)\\ &= -\left(T - T_{ref}\right)\frac{\partial}{\partial t}\left(\rho_{de;l}c_{p;de;l} + \rho_{de;g}c_{p;de;g} + \rho_s c_{p;s}\right)\\ &-L_{de}^{l\to g}\frac{\partial \rho_{de;g}}{\partial t} - \Delta H_{poly}\left(\rho_s\frac{\partial \xi}{\partial t} + \xi\frac{\partial \rho_s}{\partial t}\right)\end{aligned} \quad \text{Eq. 13}$$

3.3 Momentum conservation

A momentum equation including the gravitational acceleration, $\vec{g}$, was used to calculate the mechanical matrix velocity. For that purpose, the foam was considered as a viscous medium within which the dynamic viscosity changes with the degree of polymerization. The gas pressure *P* was calculated from the mass concentration $\rho^{a}_{de;g}$ of gaseous diethyl ether by using the ideal gas law. The momentum equation reads:

$$\frac{\partial(\rho\vec{u})}{\partial t}+\frac{1}{r}\vec{\nabla}\cdot r\left(\overline{\overline{\tau}}+(P-P_{atm})\overline{\overline{I}}+\rho\vec{u}\vec{u}\right)=\rho\vec{g} \qquad \text{Eq. 14}$$

where $\overline{\overline{\tau}}=\eta\left(-\left(\vec{\nabla}\vec{u}+\vec{\nabla}\vec{u}^{t}\right)+\frac{2}{3}\left(\vec{\nabla}\cdot\vec{u}\right)\overline{\overline{I}}\right)$ is the viscous stress tensor, η is the dynamic viscosity of the formulation and ρ is the total density.

As the gas phase is only constituted by diethyl ether, the total pressure is equal to diethyl ether pressure.

$$P = P_{de;g} \qquad \text{Eq. 15}$$

3.4 Conversion

In addition, an equation describing the conversion ξ, i.e., the dimensionless quantity accounting for the progress of reaction, was used, based on Kamal cure reaction [37–40]. It reads:

$$\frac{\partial\xi}{\partial t}=k\,\mathrm{e}^{-\frac{E_a}{RT}}(1-\xi)^{n} \qquad \text{Eq. 16}$$

where E_a is the activation energy of the polymerisation reactions and *k* is a pre-exponential factor.

3.5 Boundary and initial conditions

An axisymmetric condition was applied to the left side boundary of the foam geometry considered here, see *Figure 1*. No mass exchange with the atmosphere was considered, and a natural convective heat flux was applied to the rest of the geometry, so that:

$$-\vec{n}\cdot\left(-\lambda\vec{\nabla}T\right)=h_c\left(T_a-T\right)+\varepsilon\sigma\left(T_a^{4}-T^{4}\right) \qquad \text{Eq. 17}$$

where *n* is the normal vector, h_c is the convection heat transfer coefficient, T_a is the temperature of the air surrounding the foam, ε is the foam emissivity, and σ is the Stefan-Boltzmann constant.

Moreover, a zero velocity was imposed to the bottom boundary, whereas the top boundary was let unconstrained. The vertical boundary was allowed to move only along the vertical direction, i.e., along the direction of foam growth. This constraint was obtained by applying a force F along the radial direction. Since the model allowed a displacement of the mesh beyond the real wall of the mould, the applied force had to be proportional to the difference between the mesh position r and the wall position r_w:

$$\vec{F} = \begin{pmatrix} -F_r(r - r_w) \\ 0 \end{pmatrix} \qquad \text{Eq. 18}$$

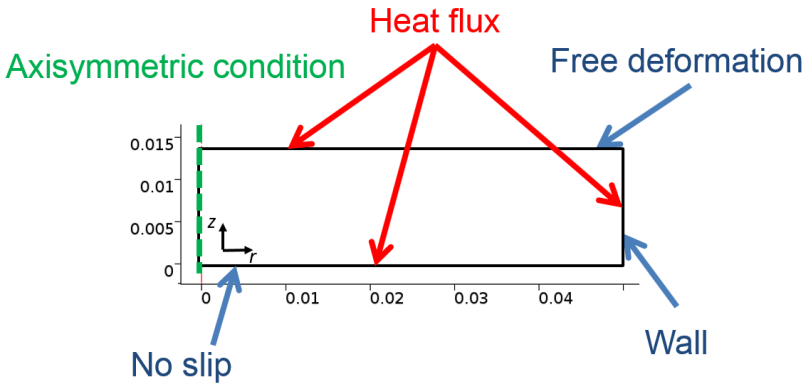

Figure 1: Initial geometry of the formulation in its cylindrical mould, and boundary conditions

Finally, all initial conditions were taken constants, according to:

$$\begin{cases} \rho_{de;l}(t=0) = \rho_{de;l;0} \\ \rho^{st}_{de;l}(t=0) = \rho_{de;l;0} \\ \rho_{de;g}(t=0) = \rho_{de;g;0} \\ \rho_s(t=0) = \rho_{s;0} \\ T(t=0) = T_0 \\ u(t=0) = u_0 \\ v(t=0) = v_0 \\ \xi(t=0) = \xi_0 \end{cases} \qquad \text{Eq. 19}$$

4 Properties and input parameters

In the previous section, a physical model was developed for simulating the expansion of tannin-based foams. This model requires the use of physical properties, input data, and values used for the initial and ambient conditions. All these necessary data are presented below.

4.1 Densities and specific heats

The skeleton is defined by an intrinsic density ρ^{i}_{s} of 1471 kg m^{-3} [41] and a specific heat capacity c_{ps} of 1680 J kg^{-1} K^{-1} (from lab measurement). The total density of the foam during growth is equal to the sum of the mass concentrations of each phase, such as:

$$\rho = \rho_s + \rho_{de;l} + \rho_{de;g} \qquad \text{Eq. 20}$$

4.2 Thermal conductivities

The thermal conductivity of the foam during expansion, λ, is described as the sum of the thermal conductivities of each phase, weighted by their corresponding volume fraction, ε (parallel model):

$$\lambda = \varepsilon_s \lambda_s + \varepsilon_{de;l} \lambda_{de;l} + \varepsilon_{de;g} \lambda_{de;g} \qquad \text{Eq. 21}$$

The thermal conductivities of diethyl ether, either in the gas phase ($\lambda_{de;g}$) or in the liquid phase ($\lambda_{de;l}$), are given in

Table 2. The thermal conductivity of the skeleton, λ_S, is taken as 0.32 W m^{-1} K^{-1} [42].

4.3 Dynamic viscosity of the polymeric matrix

The dynamic viscosity η mainly depends on the polymerisation reaction [23,25,38,43]. Since we had no measurement of the experimental viscosity as a function of time, we had to base ourselves on models existing in the literature, simplified herein in the form of a constant viscosity at the beginning of the reaction, followed by a rapid rise at some critical conversion (here 0.3). For the numerical optimisation of the model, the final value of viscosity was set to a constant. The dynamic viscosity was thus simulated with a sigmoid function. The latter defines a step-like, polymerisation-dependent viscosity, starting from a low initial value (η = 10^3 Pa.s) to simulate a fluid-like behaviour, and ending at a high viscosity (η = 10^{12} Pa.s) to simulate a solid-like foam behaviour. The hardening of the matrix has been fixed at a

conversion between 0.3 and 0.4, see *Figure 1*. The aforementioned parameters were evaluated from an internal parametric study and must be refined to precisely validate the model.

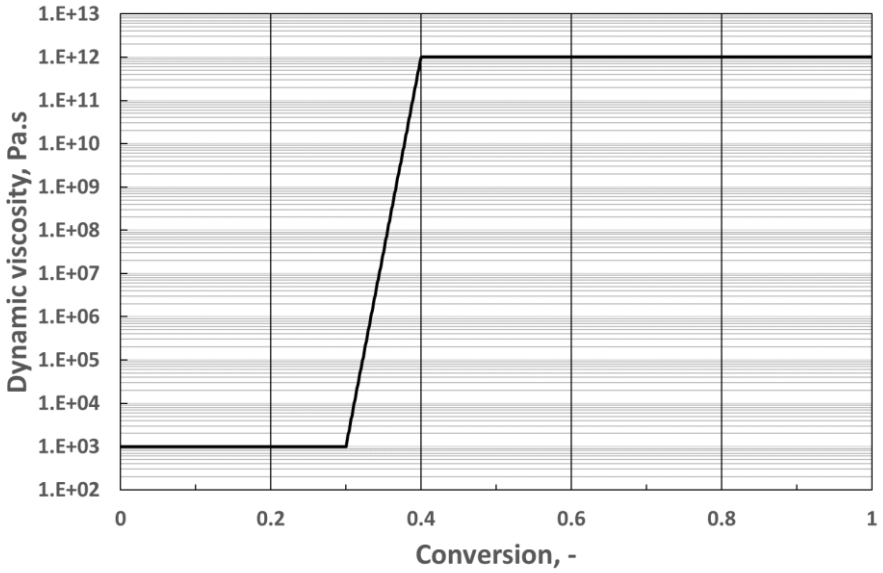

Figure 2 : Dynamic viscosity, modelled by a step function, versus conversion

*Table 2 : Initial values of variables used in the model; the * denotes the parameters that have been recalibrated from the experimental points of a previous work [34] by performing a parametric study.*

Symbol	Definition	Units	Value	Reference or comment
ΔT	Temperature range used in the function related to diethyl ether phase change	K	5	Parametric study*
$c_{p;de;g}$	Specific heat capacity of gaseous diethyl ether	J kg^{-1} K^{-1}	1606	[44]
$c_{p;de;l}$	Specific heat capacity of liquid diethyl ether	J kg^{-1} K^{-1}	2321	[45]
F_r	Force parameter simulating the wall of the beaker	N	10^7	Parametric study*
g	Gravitational acceleration	m s^{-2}	0 along r -9.81 along z	-
h_c	Convective heat transfer coefficient	W m^{-2} K^{-1}	10	[46]
ε	Foam emissivity (black body assumption)	-	1	-
H_{poly}	Enthapy of polymerisation	J kg^{-1}	-132×10^3	Parametric study*
$L^{l\rightarrow g}{}_{de}$	Heat of vaporisation of diethyl ether	J kg^{-1}	3.676×10^5	[45]

M_{de}	Molecular weight of diethyl ether	kg mol^{-1}	7.412×10^{-2}	-
P_{atm}	Atmospheric pressure	Pa	1×10^{5}	-
T_{de}	Diethyl ether boiling point	°C	34	
T_a	Air temperature	°C	20	-
$\lambda_{de;l\ ;}$	Thermal conductivity of liquid diethyl ether	W m^{-1} K^{-1}	0.18	[47]
$\lambda_{de;g}$	Thermal conductivity of the gaseous diethyl ether	W m^{-1} K^{-1}	0.018 (at 60.2°C)	[48]
$\rho^{i}_{de;l}$	Intrinsic density of liquid diethyl ether	kg m^{-3}	713.4	-
	Polymerisation function			
E_a	Activation energy	J mol^{-1}	37×10^{3}	Parametric study*
k	Pre-exponential factor	s^{-1}	15×10^{3}	Parametric study*
n	Constant	-	1.3	Parametric study*
	Initial conditions			
T_0	Initial temperature	K	293.15	Measured
$\rho_{de;l;\,0}$	Initial mass concentration of liquid diethyl ether	kg m^{-3}	44.231	Estimated from the initial formulation
$\rho_{de;g;0}$	Initial mass concentration of gaseous diethyl ether	kg m^{-3}	0.00304	Estimated from the initial formulation
$\rho_{s,0}$	Initial mass concentration of the skeleton	kg m^{-3}	1378.3	Estimated from the initial formulation
ξ_0	Initial conversion	-	0	-
$\varepsilon_{s,0}$	Initial volume fraction of the skeleton	-	0.937	Estimated from the initial formulation
$\varepsilon_{de;g;,0}$	Initial volume fraction of gaseous phase	-	0.001	Estimated from the initial formulation
$\varepsilon_{de;l,0}$	Initial volume fraction of liquid phase	-		Estimated from the initial formulation

In this model, several parameters have been recalibrated from the experimental points of a previous work [34] by performing a parametric study (denoted by a * in Table 2). Here, only the final parameters used are presented in order to highlight the construction of the model.

Indeed, new experimental developments will be made concerning the viscosity parameters, which will give a specific publication on this topic.

5 Numerical model

The 2D axisymmetric physical model was implemented with Comsol Multiphysics v5.3a commercial software using the finite element method. The initial geometry consisted of a 5 cm-wide and 1.135 cm-high rectangle, see again *Figure 1*. A mobile mesh, using the Arbitrary Lagrangian-Eulerian Method (ALE) method, composed of 28368 elements, was applied. The number of elements used was determined by performing a parametric study (see next section). Since the quality of the elements decreases with the expansion of the geometry, a remeshing was automatically done when the quality, a parameter calculated by the software, reached a minimum value of 0.1. Finally, 4 meshes were used during the simulation (*Figure 3*). In addition, some parameters were set as follows: an initial time step of 10^{-15} s and a relative tolerance of 10^{-4}.

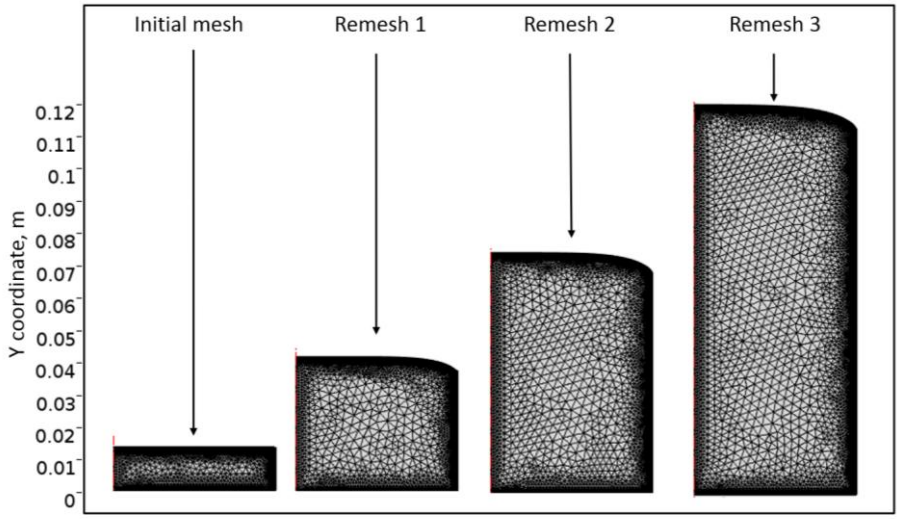

Figure 3: Different meshes used during the simulation

A parametric study on the mesh was carried out in order to determine which mesh size should be used. The mesh size on the border was fixed, and only the central mesh size was varied. Thus, 4 configurations of meshes (see *Table 3* and *Figure 4*), predefined by the software, were tested ranging from "Coarse" to "Extra fine".

Table 3: Internal element size, final element number and computation time for meshes used in the present study

Mesh	Internal element size (m)			Simulation time (s)	Final element number	Computation time
	Maximum element size	Minimum element size	Maximum element growth rate			
Coarse	0.006	3.00E-04	1.5	7200	13045	1d 2h 18min 54s
Normal	0.00335	1.50E-05	1.3	7200	14282	1d 4h 22min 7s
Fine	0.00265	1.50E-05	1.3	7200	18634	1d 13h 4min 44s
Extra fine	0.001	3.75E-06	1.2	7200	28368	2d 18h 4min 27s

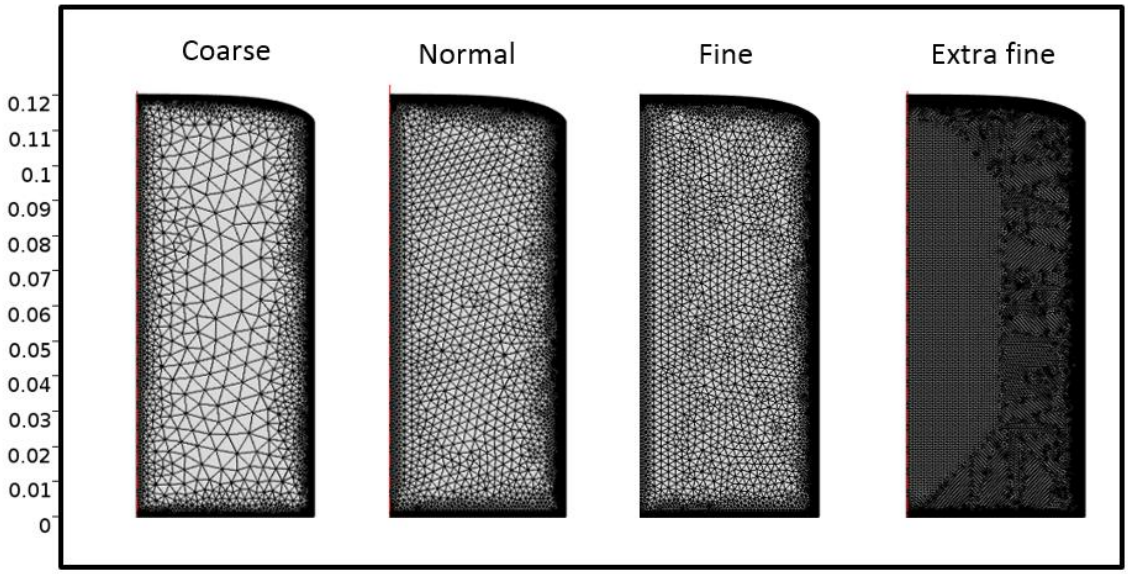

Figure 4: Meshes used for the parametric study, ranked from coarsest to finest

The different meshes had a negligible impact on foam expansion and temperature, and hence the results are not presented here. Regarding expansion for instance, *Figure 4* indeed shows that the final meshes have exactly the same shape and the same height. The situation was not the same for pressure, which is a specially interesting parameter in this type of study as it is derived from temperature calculation, material balance and mechanical equilibrium [49]. *Figure 5a* thus shows the changes of gas pressure, calculated at a central point of the simulated foam (r = 0.025 m and z = 0.00675 m), as a function of time for all the various tested meshes. It can be observed that the differences were the highest between 50 and 80 minutes. Therefore, the studies focused only on this part of the curve, and especially on the final part (i.e., after 60 minutes, see *Figure 5b*).

Figure 5b shows that the calculated pressure converged when the mesh was refined. Thus, the pressure stabilised around -6000 Pa for “coarse” meshes, around -3000 Pa for "normal" and "fine" type meshes, and around 0 Pa for an "extra fine" type mesh. The latter led to an acceptable solution because absolute gas pressure can never be under zero. To conclude on the mesh sensitivity studies, a mesh type "extra fine" was found to be acceptable and was thus chosen to present the results.

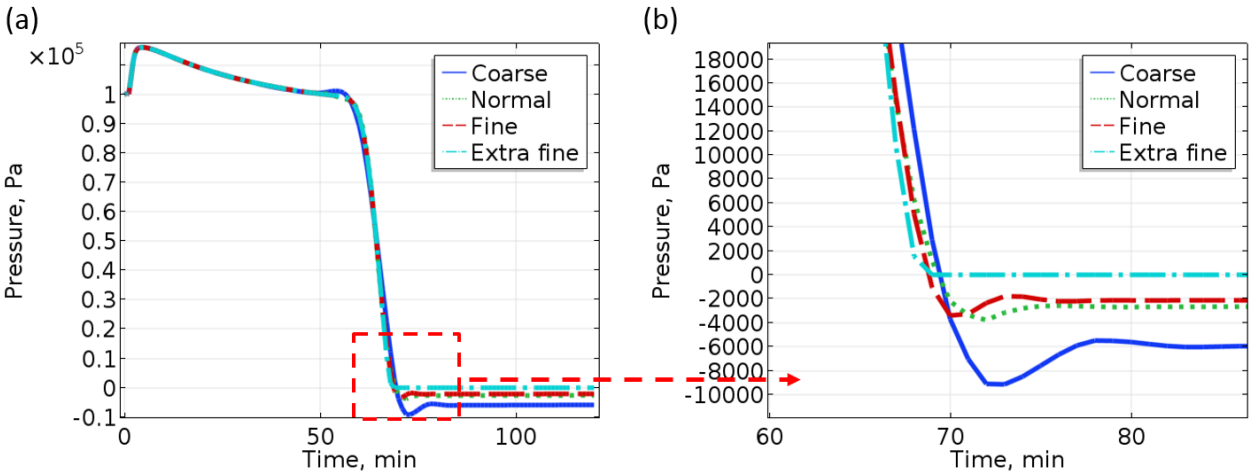

Figure 5 : (a) Temporal evolution of pressure calculated for different meshes; (b) same as (a) but with a focus on the moment when differences are observed

6 Results and discussion

In the present study, only the temperature measured at a fixed position centred on the revolution axis of the foam, and the measured height of the foam, both retrieved from a former paper [34], were taken into account and compared to the simulation.

Figure 6a shows the changes as a function of time of experimental (black squares) and calculated (solid line) temperature at 1.8 cm from the bottom of the foam on its revolution axis. The experimental evolution of the temperature shows two distinct phases: a sharp increase up to 85°C, followed by a gradual decrease down to room temperature. These two phases are also seen in the simulation. During the first three minutes, the calculated increase of the temperature was faster than the experimental one but the maximum was higher, 87.5°C, and was reached after 4 minutes of simulation, against 2 minutes in the experiment. The simulation also overestimated the temperature during the cooling phase.

The experimental evolution of height presents three phases, see *Figure 6b*. During the first one, negligible deformation is observed: the material remains liquid and there is almost no

expansion. This period corresponds to the observed induction time, which lasts for a few tens of seconds after the addition of the acid catalyst. The second phase shows a very rapid increase of foam height. Finally, during the third phase, the foam, and hence its geometry, stabilise. The calculated evolution also presented these three phases, although the first one was extremely short, about 30 seconds, against about 1 minute in the experiment. This might be due to the fact that the simulation considers a perfectly homogeneous mixture from the very beginning, whereas the (viscous) reactants need time for being intimately mixed in any real experiment. But the kinetics of expansion was similar to the experimental one, and so was the final height: 12 times the initial one for the simulation, against 11 times for the experiment.

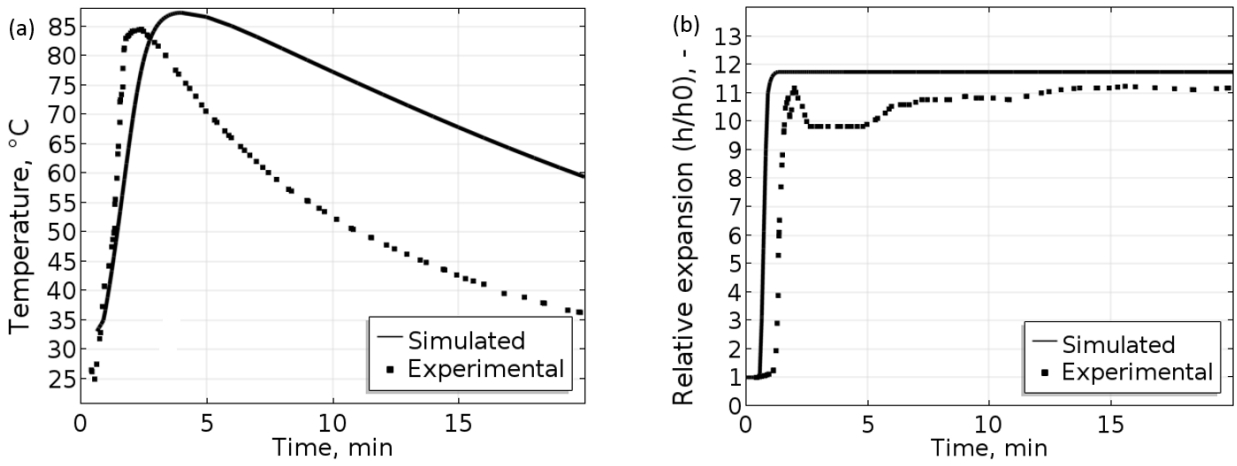

Figure 6: Evolution of: (a) experimental (black squares) and simulated (line) temperature at 1.8 cm above the bottom of the foam and on its axis of symmetry, and (b) experimental (black squares) and simulated (line) foam height.

The comparison of calculated and experimental data thus demonstrated similar overall trends. However, differences were seen, and can be explained in two ways:

(1) The viscosity and the polymerisation equation used here were inspired from the bibliography related to polyurethane foams (see again *Table* 2). It would be interesting to develop experimental tools for carrying out our own measurements and getting parameters corresponding to the present tannin-based foams.

(2) The experimental data of temperature at one point of the foam and of foam expansion, as a function of time, were taken from one paper of the literature, for which not all precise measurement conditions were given, such as air temperature, initial height,

mixing time, repeatability, etc. The development of a dedicated experimental device for controlling these unknowns appears necessary for validating the model and improving it further.

Whereas the foaming mechanism of tannin-based formulations is qualitatively well understood, as explained in section 2, the phenomena highlighted by our model deserve further discussion. Indeed, even if the present simulation can be considered as realistic despite the obvious discrepancies already observed in *Figure 6*, some deviations from the experimental data can be justified as soon as one considers the way the model was designed.

Figure 7 thus shows the temporal evolution of quantities calculated from the model for three points A, B and C along the vertical revolution axis of the foam (see the inset in *Figure 7c*). These three points were chosen in the lower, middle, and upper part, and were mobile, i.e., their positions change depending on the expansion of the material. The results of *Figure 7* are given for the first 120 min of the foaming process, except for mass concentration and volume fraction of each phase, for which only the first minute of simulation is presented in order to highlight the expansion phenomenon (*Figure 7e* and *Figure 7f*, respectively).

The present model is based on the conservation of mass, momentum and energy. As shown by the momentum conservation equation (Eq. 16), the increase of pressure is the driving force of the expansion. In the very first moments of the foaming, the abrupt increase of temperature (*Figure 7a*), due to the exothermic nature of the polymerisation reaction, induced a drop of mass concentration of liquid diethyl ether (*Figure 7c*), due to its change of state. As a result, the mass concentration of the gaseous diethyl ether increased sharply at $t < 1$ min (*Figure 7d*), resulting in a pressure increase (*Figure 7b*). Focusing on the pressure evolution between 0 and 4 minutes, the calculation produced two peaks of pressure (*Figure 8a*): one between 0.5 and 1 minute and the other above 1 minute. It can also be observed that the increase of volume, also presented in *Figure 8a*, only depends on the first peak of pressure. Indeed, during this period, the pressure increases as a result of phase change, then decreases due to the expansion allowed by the still low viscosity of the porous matrix. The second increase in pressure occurs whereas the foam is completely stiffened (compare *Figure 8a* and *Figure 8b*). Then, the pressure generated by the rise of temperature can no longer decrease due to the high viscosity of the medium (*Figure 8b*). As a result, the pressure continuously increases until a plateau reached at $t \approx 4$ min, at which the temperature goes through a maximum (*Figure 7a*) corresponding to the end of the exothermic reaction (*Figure 8b*). This simulation highlights a

questionable choice of the viscosity model. Indeed, it is unlikely that the expansion occurs when the viscosity is the lowest, but at intermediate values allowing both the development and the stabilisation of the structure. However, this simplifying way of "modelling" the viscosity makes it possible to authorise, or not, the deformation of the material. Finally, it can be seen that the relative expansion is definitively stopped when the viscosity is at its maximum value. The latter plays its role well because the material could continue to expand with the temperature that increases further after the end of the expansion, a consequence of the reaction, which is not completed.

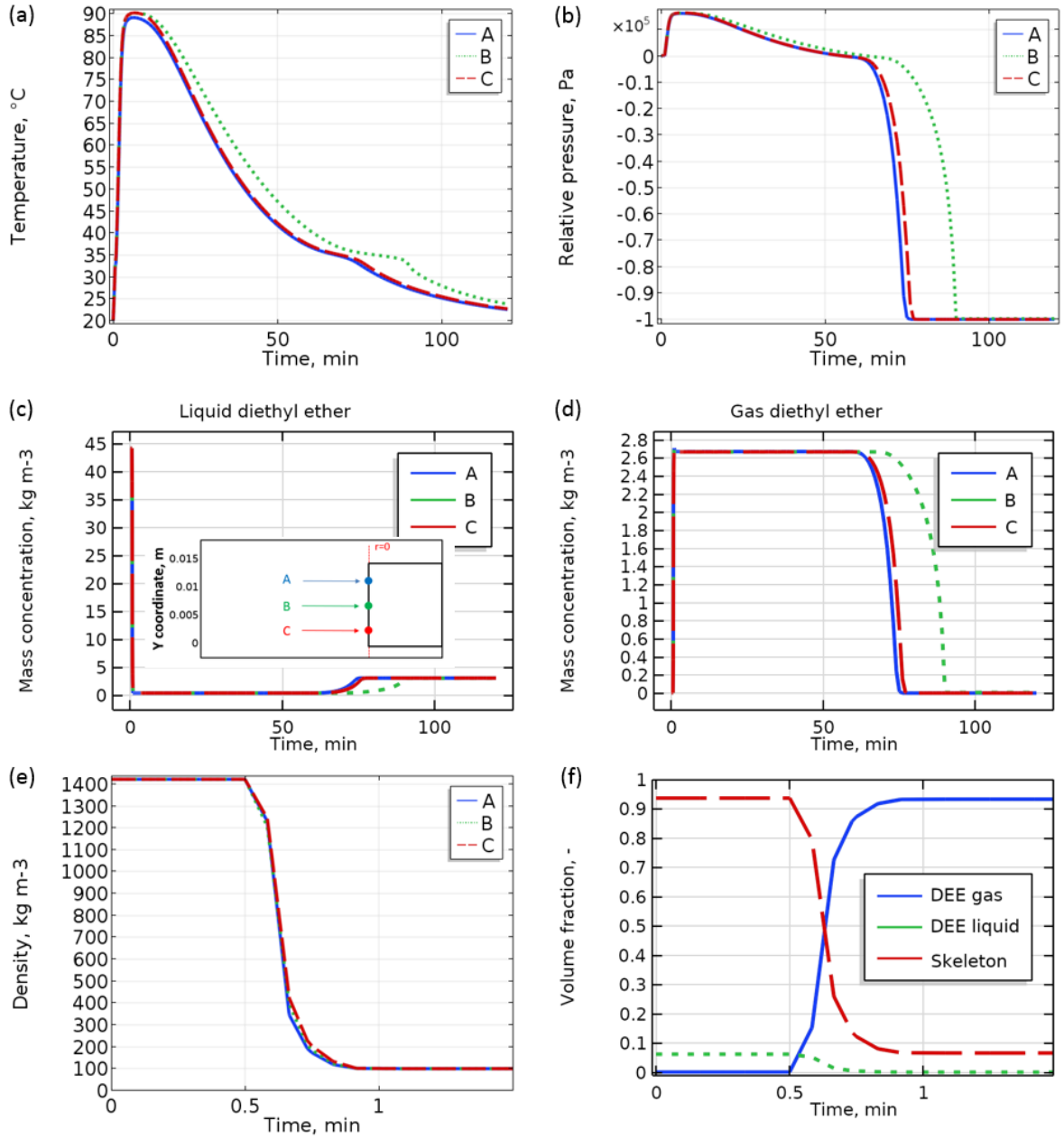

Figure 7 : Calculated temporal evolution of: (a) temperature; (b) relative pressure with respect to atmosphere; (c) mass concentration of liquid diethyl ether, (d) mass concentration of gaseous diethyl ether; (e) foam density; and (f) volume fraction of each phase.

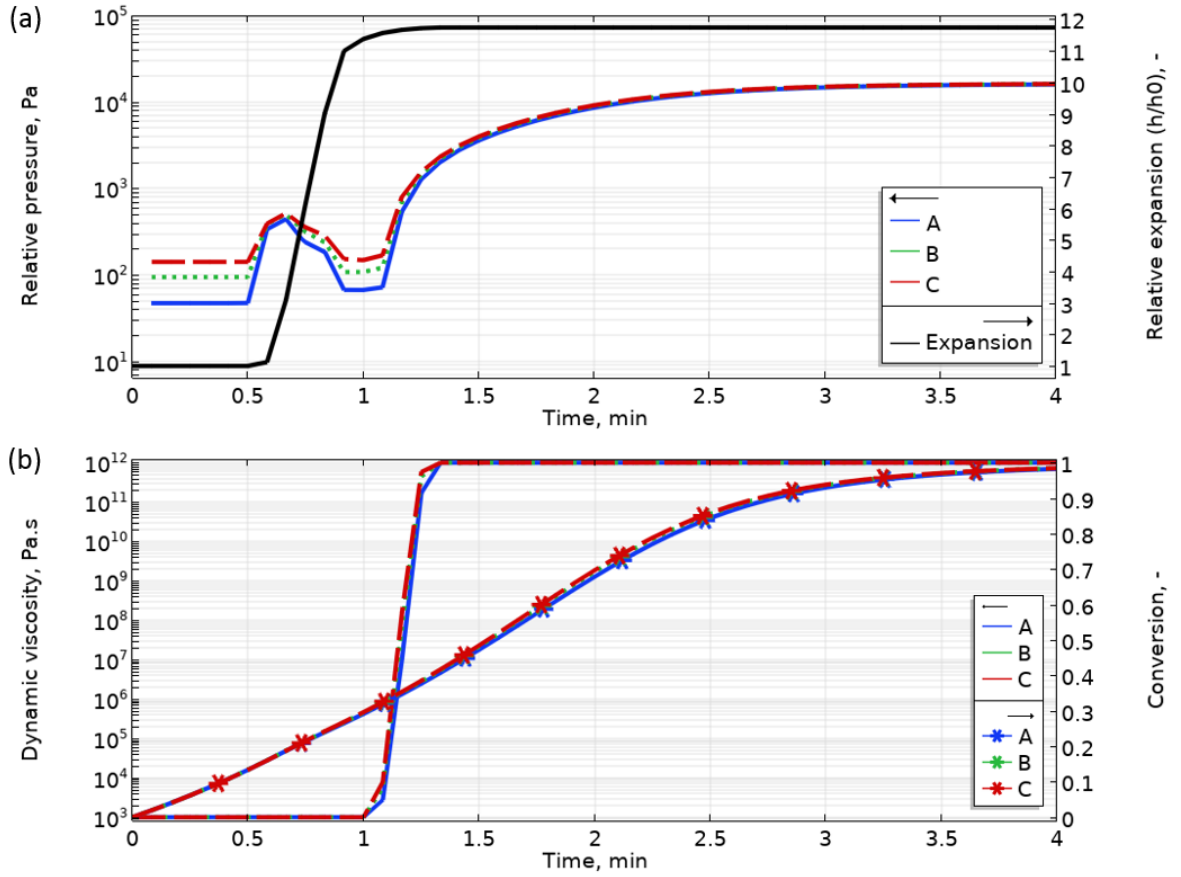

Figure 8 : Calculated values of: (a) relative pressure (left scale) and relative expansion (right scale), and (b) dynamic viscosity (left scale) and conversion (right scale).

The evolutions of the density of the foam (*Figure 7e*) and of the volume fractions of each phase (*Figure 7f*) provide more information on the modelling of the expansion phenomenon. This was verified in *Figure 7f* where it can be seen that the volume fraction of gas phase (from 0 to 92 %) is compensated by the corresponding decrease of those of skeleton (from 94 to 8 %) and liquid (from 6 to nearly 0 %) phases. Such increase of the volume fraction of gas phase up to 92 % created the porosity, hence the corresponding decrease of foam density (*Figure 7e*).

Once the porous matrix was stiff and once polymerisation reactions were completed, the temperature decreased by heat losses with the outside air at room temperature (*Figure 7a*). During the decrease of temperature, a discontinuity related to the condensation of the gaseous diethyl ether that could not escape the foam is observed. Such change of state was confirmed

by the curves of mass concentration of liquid and gaseous diethyl ether, which increased and decreased, respectively (*Figure 7c* and *Figure 7d*, respectively). Upon condensation, the liquid mass concentration did not reach the initial value at $t = 0$ and remained at a level of about 3 kg m^{-3} because, after expansion, there was obviously less matter per cubic meter of product.

In parallel, the condensation of diethyl ether induced a decrease of pressure, which passed below the atmospheric pressure (*Figure 7b*). The model indeed assumed that the pores are closed, which is not necessarily the case in reality with such expansion. An open porosity would allow a transfer of gas from the atmosphere by depression (Darcy's law) and diffusion (Fick's law) (unless the porosity opens before the condensation occurs, so that the gas would move out from the pores toward the atmosphere), thus stabilising the pressure at the atmospheric value at the end. Nevertheless, the careful observation of experimental foaming of tannin-based formulation evidenced some shrinkage, which might be related to the condensation-induced depression in the pores, and/or to the decrease of the temperature (ideal gas law effect).

7 Conclusion

In this paper, a multi-physical model was introduced with the aim of simulating the foaming of a standard tannin-based formulation at the lab scale. This 2D axisymmetric model, implemented on a mobile mesh with Comsol Multiphysics v5.3a commercial software, allowed calculating the changes of temperature, the mass transfers, the expansion of the material, and the progress of the polymerisation reactions. The important multi-physical couplings and phenomena that normally occur during the foaming process were taken into account through realistic equations and relevant properties. A parametric study on the mesh was carried out in order to determine which mesh size was the most appropriate. A mesh size type "extra fine" was chosen.

Calculated and experimental data were compared, and similar trends were globally observed, even if discrepancies were also noticed. Validating the model and improving it further will thus require two new developments to be performed in the near future: (i) getting more accurate data from polymerisation studies of tannin-based resins, that are still missing today; and (ii) building our own device for measuring simultaneously, and in a continuous

way as a function of time, the temperature at different positions inside the foam in the growth phase, the expansion, and the mass of the foam.

The results from the numerical model have shown that the expansion of the material is mainly due to the increase of inner gas pressure, generated by the change of state of the blowing agent from liquid to vapour when the temperature exceeds its boiling point. The results, although in fair agreement with the experimental results, also proved the need of refining the model by introducing a phenomenon of pore opening, in order to limit the condensation of diethyl ether during the cooling of the foam. The corresponding work is underway, in which a sensitivity study will have to be carried out to highlight the impact of the estimated parameters, whereas in the present article, the authors had only wanted to emphasize the simple development of the model.

8 Notations

Greek symbols

ΔT	Temperature range used in the function related to the change of phase of diethyl ether, K
ε	Emissivity of the foam, dimensionless
ε_s	Volume fraction of the skeleton, $m^3\ m^{-3}$
$\varepsilon_{de;l}$	Volume fraction of liquid diethyl ether, $m^3\ m^{-3}$
$\varepsilon_{de;g}$	Volume fraction of gaseous diethyl ether, $m^3\ m^{-3}$
η	Dynamic viscosity, Pa s
λ	Thermal conductivity, $W\ m^{-1}\ K^{-1}$
ξ	Conversion, dimensionless
ρ	Density or mass concentration, $kg\ m^{-3}$
σ	Stefan-Boltzmann constant, $W\ m^{-2}\ K^{-4}$
$\bar{\bar{\tau}}$	Viscous stress, Pa

Letters

c_p	Specific heat, J kg^{-1} K^{-1}
E_a	Activation energy, J mol^{-1}
F	Force, N
$\vec{g}$	Gravitational acceleration, m s^{-2}
h_c	Convection heat transfer coefficient, W m^{-2} K^{-1}
H	Volume enthalpy, J m^{-3}
H_{poly}	Enthalpy of polymerization, J kg^{-1}
$\bar{\bar{I}}$	Identity matrix
K	Phase change function, kg m^{-3} s^{-1}
k	Pre-exponential factor, s^{-1}
L	Latent heat of vaporisation, J kg^{-1}
M	Molecular weight, kg mol^{-1}
n	Polymerisation exponent
	Normal vector
P	Pressure, Pa
$\vec{\dot{Q}}$	Conduction heat flux, J m^{-2} s^{-1}
R	Ideal gas constant, J mol^{-1} K^{-1}
r	Radius of the cylindrical mould for foaming, m
T	Temperature, K
t	Time, s
$\vec{u}$	Velocity, m s^{-1}

Subscript

0	Initial
atm	Atmosphere
c	Convection

de	Diethyl ether
g	Gas
l	Liquid
ref	Reference
s	Skeleton
w	Wall

Superscript

i	Intrinsic
st	Amount of liquid diethyl ether able of phase change

Acknowledgement

Dr Yves Jannot from LEMTA - UMR CNRS Université de Lorraine n°7563 is thanked for measuring and providing the value of Cp used in the present work.

References

[1] V. Srivastava, R. Srivastava, On the polymeric foams: modeling and properties, J. Mater. Sci. 49 (2014) 2681–2692. https://doi.org/10.1007/s10853-013-7974-5.

[2] S.A. Baser, D.V. Khakhar, Modeling of the Dynamics of Water and R-11 blown polyurethane foam formation, Polym. Eng. Sci. 34 (1994) 642–649. https://doi.org/10.1002/pen.760340805.

[3] S.A. Baser, D.V. Khakhar, Modeling of the dynamics of R-11 blown polyurethane foam formation, Polym. Eng. Sci. 34 (1994) 632–641. https://doi.org/10.1002/pen.760340804.

[4] M.C. Basso, L. Delmotte, F. Al-Marzouki, S. Abdalla, A. Celzard, MALDI-TOF and 13C NMR Analysis of Tannin–Furanic–Polyurethane Foams Adapted for Industrial Continuous Lines Application, Polymers. 6 (2014) 2985–3004. https://doi.org/10.3390/polym6122985.

[5] M.C. Basso, M.-C. Lagel, A. Pizzi, A. Celzard, S. Abdalla, First Tools for Tannin-Furanic Foams Design, BioResources. 10 (2015). https://doi.org/10.15376/biores.10.3.5233-5241.

[6] X. Li, M.C. Basso, V. Fierro, A. Pizzi, A. Celzard, Chemical Modification of Tannin/Furanic Rigid Foams by Isocyanates and Polyurethanes, Maderas Cienc. Tecnol. (2012) 0–0. https://doi.org/10.4067/S0718-221X2012005000001.

[7] D.A. Babb, Polyurethanes from Renewable Resources, in: B. Rieger, A. Künkel, G.W. Coates, R. Reichardt, E. Dinjus, T.A. Zevaco (Eds.), Synth. Biodegrad. Polym., Springer Berlin Heidelberg, Berlin, Heidelberg, 2011: pp. 315–360. https://doi.org/10.1007/12_2011_130.

[8] C.K. Lyon, V.H. Garrett, E.N. Frankel, Rigid urethane foams from hydroxymethylated castor oil, safflower oil, oleic safflower oil, and polyol esters of castor acids, J. Am. Oil Chem. Soc. 51 (1974) 331–334.
[9] A. Lee, Y. Deng, Green polyurethane from lignin and soybean oil through non-isocyanate reactions, Eur. Polym. J. 63 (2015) 67–73. https://doi.org/10.1016/j.eurpolymj.2014.11.023.
[10] J.-M. Raquez, M. Deléglise, M.-F. Lacrampe, P. Krawczak, Thermosetting (bio)materials derived from renewable resources: A critical review, Prog. Polym. Sci. 35 (2010) 487–509. https://doi.org/10.1016/j.progpolymsci.2010.01.001.
[11] W.S. Ng, C.S. Lee, C.H. Chuah, S.-F. Cheng, Preparation and modification of water-blown porous biodegradable polyurethane foams with palm oil-based polyester polyol, Ind. Crops Prod. 97 (2017) 65–78. https://doi.org/10.1016/j.indcrop.2016.11.066.
[12] N. Mahmood, Z. Yuan, J. Schmidt, C. (Charles) Xu, Depolymerization of lignins and their applications for the preparation of polyols and rigid polyurethane foams: A review, Renew. Sustain. Energy Rev. 60 (2016) 317–329. https://doi.org/10.1016/j.rser.2016.01.037.
[13] A. Guo, I. Javni, Z. Petrovic, Rigid polyurethane foams based on soybean oil, J. Appl. Polym. Sci. 77 (2000) 467–473.
[14] H. Li, C. (Charles) Xu, Z. Yuan, Q. Wei, Synthesis of bio-based polyurethane foams with liquefied wheat straw: Process optimization, Biomass Bioenergy. 111 (2018) 134–140. https://doi.org/10.1016/j.biombioe.2018.02.011.
[15] N.E. Meikleham, A. Pizzi, Acid-and alkali-catalyzed tannin-based rigid foams, J. Appl. Polym. Sci. 53 (1994) 1547–1556.
[16] H. Al-Moameri, Y. Zhao, R. Ghoreishi, G.J. Suppes, Simulation of liquid physical blowing agents for forming rigid urethane foams, J. Appl. Polym. Sci. 132 (2015) n/a-n/a. https://doi.org/10.1002/app.42454.
[17] P. Ferkl, M. Karimi, D.L. Marchisio, J. Kosek, Multi-scale modelling of expanding polyurethane foams: Coupling macro- and bubble-scales, Chem. Eng. Sci. 148 (2016) 55–64. https://doi.org/10.1016/j.ces.2016.03.040.
[18] M. Karimi, D.L. Marchisio, A Baseline Model for the Simulation of Polyurethane Foams via the Population Balance Equation, Macromol. Theory Simul. 24 (2015) 291–300. https://doi.org/10.1002/mats.201500014.
[19] L. Shen, Y. Zhao, A. Tekeei, F.-H. Hsieh, G.J. Suppes, Density modeling of polyurethane box foam, Polym. Eng. Sci. 54 (2014) 1503–1511. https://doi.org/10.1002/pen.23694.
[20] Y. Zhao, M.J. Gordon, A. Tekeei, F.-H. Hsieh, G.J. Suppes, Modeling reaction kinetics of rigid polyurethane foaming process, J. Appl. Polym. Sci. 130 (2013) 1131–1138. https://doi.org/10.1002/app.39287.
[21] M. Karimi, H. Droghetti, D.L. Marchisio, PUFoam : A novel open-source CFD solver for the simulation of polyurethane foams, Comput. Phys. Commun. 217 (2017) 138–148. https://doi.org/10.1016/j.cpc.2017.03.010.
[22] M. Karimi, H. Droghetti, D.L. Marchisio, Multiscale Modeling of Expanding Polyurethane Foams via Computational Fluid Dynamics and Population Balance Equation, Macromol. Symp. 360 (2016) 108–122. https://doi.org/10.1002/masy.201500108.
[23] J. Bikard, J. Bruchon, T. Coupez, L. Silva, Numerical simulation of 3D polyurethane expansion during manufacturing process, Colloids Surf. Physicochem. Eng. Asp. 309 (2007) 49–63. https://doi.org/10.1016/j.colsurfa.2007.04.025.
[24] J. Bikard, J. Bruchon, T. Coupez, B. Vergnes, Numerical prediction of the foam structure of polymeric materials by direct 3D simulation of their expansion by chemical

reaction based on a multidomain method, J. Mater. Sci. 40 (2005) 5875–5881. https://doi.org/10.1007/s10853-005-5022-9.
[25] I.E. Ireka, D. Niedziela, K. Schäfer, J. Tröltzsch, K. Steiner, F. Helbig, T. Chinyoka, L. Kroll, Computational modelling of the complex dynamics of chemically blown polyurethane foam, Phys. Fluids 1994-Present. 27 (2015) 113102. https://doi.org/10.1063/1.4935788.
[26] R. Rao, L. Mondy, D. Noble, V. Brunini, K. Long, C. Roberts, N. Wyatt, M. Celina, K. Thompson, J. Tinsley, Density predictions using a finite element/level set model of polyurethane foam expansion and polymerization, Comput. Fluids. 175 (2018) 20–35. https://doi.org/10.1016/j.compfluid.2018.08.010.
[27] H. Abdessalam, B. Abbès, F. Abbès, Y. Li, Y.-Q. Guo, Prediction of acoustic properties of polyurethane foams from the macroscopic numerical simulation of foaming process, Appl. Acoust. 120 (2017) 129–136. https://doi.org/10.1016/j.apacoust.2017.01.021.
[28] G. Tondi, S. Blacher, A. Léonard, A. Pizzi, V. Fierro, J.M. Leban, A. Celzard, X-Ray Microtomography Studies of Tannin-Derived Organic and Carbon Foams, Microsc. Microanal. 15 (2009) 384–394. https://doi.org/10.1017/S1431927609990444.
[29] G. Tondi, W. Zhao, A. Pizzi, G. Du, V. Fierro, A. Celzard, Tannin-based rigid foams: a survey of chemical and physical properties, Bioresour. Technol. 100 (2009) 5162–5169. https://doi.org/10.1016/j.biortech.2009.05.055.
[30] G. Tondi, A. Pizzi, Tannin-based rigid foams: Characterization and modification, Ind. Crops Prod. 29 (2009) 356–363. https://doi.org/10.1016/j.indcrop.2008.07.003.
[31] W. Zhao, A. Pizzi, V. Fierro, G. Du, A. Celzard, Effect of composition and processing parameters on the characteristics of tannin-based rigid foams. Part I: Cell structure, Mater. Chem. Phys. 122 (2010) 175–182. https://doi.org/10.1016/j.matchemphys.2010.02.062.
[32] W. Zhao, V. Fierro, A. Pizzi, G. Du, A. Celzard, Effect of composition and processing parameters on the characteristics of tannin-based rigid foams. Part II: Physical properties, Mater. Chem. Phys. 123 (2010) 210–217. https://doi.org/10.1016/j.matchemphys.2010.03.084.
[33] A. Celzard, V. Fierro, G. Amaral-Labat, A. Pizzi, J. Torero, Flammability assessment of tannin-based cellular materials, Polym. Degrad. Stab. 96 (2011) 477–482. https://doi.org/10.1016/j.polymdegradstab.2011.01.014.
[34] M.C. Basso, A. Pizzi, A. Celzard, Dynamic Foaming Behaviour of Polyurethane vs Tannin/Furanic Foams, J. Renew. Mater. 1 (2013) 273–278. https://doi.org/10.7569/JRM.2013.634125.
[35] A. Szczurek, G. Amaral-Labat, V. Fierro, A. Pizzi, E. Masson, A. Celzard, The use of tannin to prepare carbon gels. Part I: Carbon aerogels, Carbon. 49 (2011) 2773–2784. https://doi.org/10.1016/j.carbon.2011.03.007.
[36] M. Dal, P. Le Masson, M. Carin, Estimation of fusion front in 2D axisymmetric welding using inverse method, Int. J. Therm. Sci. 55 (2012) 60–68. https://doi.org/10.1016/j.ijthermalsci.2011.12.010.
[37] R.R. Rao, L.A. Mondy, D.R. Noble, H.K. Moffat, D.B. Adolf, P. k. Notz, A level set method to study foam processing: a validation study, Int. J. Numer. Methods Fluids. 68 (2012) 1362–1392. https://doi.org/10.1002/fld.2671.
[38] F. Dimier, N. Sbirrazzuoli, B. Vergnes, M. Vincent, Etude rhéocinétique d'un système polyuréthane, in: 37ème Congrès Groupe Fr. Rhéologie, Groupe français de Rhéologie, 2002: pp. 6–pages. https://hal.archives-ouvertes.fr/hal-00579411/ (accessed December 12, 2016).
[39] P.J. Halley, M.E. Mackay, Chemorheology of thermosets—an overview, Polym. Eng. Sci. 36 (1996) 593–609.

[40] M.R. Kamal, S. Sourour, Kinetics and thermal characterization of thermoset cure, Polym. Eng. Sci. 13 (1973) 59–64.
[41] C. Lacoste, M. Čop, K. Kemppainen, S. Giovando, A. Pizzi, M.-P. Laborie, M. Sernek, A. Celzard, Biobased foams from condensed tannin extracts from Norway spruce (Picea abies) bark, Ind. Crops Prod. 73 (2015) 144–153. https://doi.org/10.1016/j.indcrop.2015.03.089.
[42] C. Lacoste, A. Pizzi, M.-P. Laborie, A. Celzard, Pinus pinaster tannin/furanic foams: Part II. Physical properties, Ind. Crops Prod. 61 (2014) 531–536. https://doi.org/10.1016/j.indcrop.2014.04.034.
[43] H. Abdessalam, B. Abbès, Y. Li, Y.Q. Guo, E. Kwassi, J.L. Romain, Simulation of polyurethane foam expansion with finite pointset and volume of fluid methods: implementation and experimental validation, Mater. Res. Innov. 19 (2015) S8-149-S8-156. https://doi.org/10.1179/1432891715Z.0000000001646.
[44] J. Chao, K.R. Hall, K.N. Marsh, R.C. Wilhoit, Thermodynamic properties of key organic oxygen compounds in the carbon range C1 to C4. Part 2. Ideal gas properties, J. Phys. Chem. Ref. Data. 15 (1986) 1369–1436.
[45] J.F. Counsell, D.A. Lee, J.F. Martin, Thermodynamic properties of organic oxygen compounds. Part XXVI. Diethyl ether, J. Chem. Soc. Inorg. Phys. Theor. (1971) 313–316.
[46] V. Nicolas, F. Vanin, D. Grenier, T. Lucas, C. Doursat, D. Flick, Modeling bread baking with focus on overall deformation and local porosity evolution, AIChE J. 62 (2016) 3847–3863. https://doi.org/10.1002/aic.15301.
[47] X. Li, J. Wu, Q. Dang, Thermal Conductivity of Liquid Diethyl Ether, Diisopropyl Ether, and Di- *n* -butyl Ether from (233 to 373) K at Pressures up to 30 MPa, J. Chem. Eng. Data. 55 (2010) 1241–1246. https://doi.org/10.1021/je900615b.
[48] R.G. Vines, L.A. Bennett, The Thermal Conductivity of Organic Vapors. The Relationship between Thermal Conductivity and Viscosity, and the Significance of the Eucken Factor, J. Chem. Phys. 22 (1954) 360–366. https://doi.org/10.1063/1.1740075.
[49] V. Nicolas, P. Salagnac, P. Glouannec, J.-P. Ploteau, V. Jury, L. Boillereaux, Modelling heat and mass transfer in deformable porous media: Application to bread baking, J. Food Eng. 130 (2014) 23–35. https://doi.org/10.1016/j.jfoodeng.2014.01.014.